

Magnetic Resonance Imaging System–Driven Medical Robotics

Onder Erin, Mustafa Boyvat, Mehmet Efe Tiryaki, Martin Phelan, and Metin Sitti*

Magnetic resonance imaging (MRI) system–driven medical robotics is an emerging field that aims to use clinical MRI systems not only for medical imaging but also for actuation, localization, and control of medical robots. Submillimeter scale resolution of MR images for soft tissues combined with the electromagnetic gradient coil–based magnetic actuation available inside MR scanners can enable theranostic applications of medical robots for precise image-guided minimally invasive interventions. MRI-driven robotics typically does not introduce new MRI instrumentation for actuation but instead focuses on converting already available instrumentation for robotic purposes. To use the advantages of this technology, various medical devices such as untethered mobile magnetic robots and tethered active catheters have been designed to be powered magnetically inside MRI systems. Herein, the state-of-the-art progress, challenges, and future directions of MRI-driven medical robotic systems are reviewed.

toward semi- and fully autonomous minimally invasive robotic surgeries.^[1,2]

Medical robots require proper medical imaging feedback for accurate and safe operations due to the dynamic and unstructured environment inside or on the human body. This imaging feedback is typically used to create a quick response to unexpected dynamics of the environment or for correcting the robot motions. The medical images also provide monitoring opportunity for the surgeons during the operations. Magnetic resonance imaging (MRI) devices are one of the most widely available imaging modalities in hospitals, where 12 of 100 patients received an MRI scan in the USA in 2017.^[3] Such devices are capable of acquiring anatomical soft tissue images with high spatial and

1. Introduction

Minimally invasive medical surgeries combined with intraoperative imaging have allowed surgeons to operate confidently without having a direct line of sight to inner regions of the human body. In the absence of any imaging feedback, the surgeon is blind and cannot proceed with operations that require accuracy and repeatability. In addition, the presence of body motions makes such imaging modalities vital components for precise, safe, and robust control of robotic systems that pave the way

temporal resolution. In addition to such anatomical images, various MRI imaging techniques, including perfusion, diffusion, and functional MRI (fMRI) images, could potentially increase the level of information acquired. MRI systems can also be combined with other medical imaging modalities, such as positron emission tomography (PET), ultrasound, and electroencephalogram (EEG), to acquire diverse diagnostic information.


Clinical human MRI systems rely on very high 1D uniform magnetic fields (of the order of 1.5–7 T) and 3D magnetic field gradients (up to 20–66 mT m⁻¹ continuously^[4]). Such magnetic fields do not introduce considerable health risks, as opposed to computerized tomography (CT), X-ray, and PET imaging modalities, which expose the patients to ionizing or radioactive radiation. In addition to imaging, MRI scanners can be used for wireless actuation of magnetic robots by applying magnetic pulling forces on such robots using inherently available 3D electromagnetic gradient coils of MR scanners. In recent years, many researchers have been utilizing such a wireless magnetic actuation method for various medical robots inside MRI systems.^[5–26] This innovative use of MRI scanners could convert conventional diagnostic MR scanners into therapeutic and even theranostic clinical devices, without the introduction of an additional hardware, as shown in **Figure 1**.

This Review on MRI-driven medical robotic systems, which is a newly emerging robotics field, is structured as follows. Section 2 presents the literature with the physics of various actuation methodologies being used by MRI-driven robotics. Section 3 focuses on imaging and tracking capabilities of such MRI systems. Section 4 presents an overview of MRI-driven medical robots. Section 5 focuses on system-level study of MRI systems as a robotic platform, Section 6 introduces the safety concerns, and

O. Erin, Dr. M. Boyvat, M. E. Tiryaki, M. Phelan, Prof. M. Sitti
 Physical Intelligence Department
 Max Planck Institute for Intelligent Systems
 Stuttgart 70569, Germany
 E-mail: sitti@is.mpg.de

O. Erin, M. Phelan, Prof. M. Sitti
 Mechanical Engineering Department
 Carnegie Mellon University
 Pittsburgh, PA 15213, USA

Prof. M. Sitti
 School of Engineering and School of Medicine
 Koç University
 Istanbul 34450, Turkey

 The ORCID identification number(s) for the author(s) of this article can be found under <https://doi.org/10.1002/aisy.201900110>.

© 2020 The Authors. Published by WILEY-VCH Verlag GmbH & Co. KGaA, Weinheim. This is an open access article under the terms of the Creative Commons Attribution License, which permits use, distribution and reproduction in any medium, provided the original work is properly cited.

DOI: 10.1002/aisy.201900110

Section 7 presents current challenges, future directions, and a brief summary of MRI-driven robotics.

2. Magnetic Actuation Methods inside MR Scanners

2.1. Gradient Pulling–Based Magnetic Actuation

A typical gradient coil unit in MRI systems consists of two sets of Golay coils and one set of Maxwell coil. Spatial magnetic field perturbations created by Golay and Maxwell coils can be represented as $\left[\frac{\partial B_x}{\partial x} \quad \frac{\partial B_y}{\partial y} \quad \frac{\partial B_z}{\partial z} \right]^T$, which are used for slice selection, phase encoding, and frequency encoding during a typical imaging sequence. These magnetic gradients used for imaging can also be used for actuation of robots/devices with ferrous materials within MRI devices by exerting magnetic gradient forces, \vec{F}_{gp} . The equation for exerted magnetic gradient pulling forces can be given as

$$\vec{F}_{gp} = V(\vec{M} \cdot \nabla)\vec{B} \quad (1)$$

where V is the volume of the ferrous robot body, \vec{M} is the average magnetization vector of the ferrous object, ∇ is the vector differential operator, and \vec{B} is the magnetic field vector.

2.1.1. Gradient Pulling via Gradient Coil Units

The main magnetic field, \vec{B}_0 , is always present and along the z-axis of the MRI devices. This field is strong enough to saturate ferrous objects within MRI. Due to such saturation, the magnetization direction of the ferrous objects points in the same direction as \vec{B}_0 . This magnetic alignment imposes the magnetization vector of any ferrous object in MRI devices as

$$\vec{M} = [0 \quad 0 \quad M_s]^T \quad (2)$$

where M_s is the saturation magnetization of a ferrous object inside an MRI device. In addition, any robot body with complex nonuniform magnetization profiles would be remagnetized along the z-axis immediately after being subjected to a very high \vec{B}_0 field (e.g., 7 T). Therefore, magnetic robots with complex magnetization profiles cannot maintain their designed magnetization profiles.^[27–31] Inserting Equation (2) into Equation (1) with the given operator $\nabla = \left[\frac{\partial}{\partial x} \quad \frac{\partial}{\partial y} \quad \frac{\partial}{\partial z} \right]^T$ yields

$$\vec{F}_{gp} = VM_s \left[\frac{\partial B_x}{\partial z} \quad \frac{\partial B_y}{\partial z} \quad \frac{\partial B_z}{\partial z} \right] \quad (3)$$

Maxwell equations state $\nabla \cdot \vec{B} = 0$ and $\nabla \times \vec{B} = 0$ at any given point outside of the coil conductors under quasi-static conditions.^[9] This results in $\frac{\partial B_x}{\partial z} = \frac{\partial B_z}{\partial x}$, and $\frac{\partial B_y}{\partial z} = \frac{\partial B_z}{\partial y}$, which modifies Equation (3) as

$$\vec{F}_{gp} = VM_s \left[\frac{\partial B_z}{\partial x} \quad \frac{\partial B_z}{\partial y} \quad \frac{\partial B_z}{\partial z} \right] \quad (4)$$



Onder Erin received his B.Sc. degree in mechatronics engineering from Sabanci University, Istanbul, Turkey, in 2014. He is a Ph.D. student in the Mechanical Engineering Department, Carnegie Mellon University, Pittsburgh, PA, USA. He is currently conducting research in the Physical Intelligence Department at the Max Planck Institute for Intelligent Systems in Stuttgart, Germany. His research interests include medical robotics, mobile and soft robotics, and medical applications of robotic systems.



Mehmet Efe Tiryaki received his B.Sc. degrees in mechanical engineering and physics from Middle East Technical University, Ankara, Turkey, in 2016, and his M.Sc. degree in mechanical engineering from Swiss Federal Institute of Technology in Zurich, Switzerland, in 2018. He is currently a Ph.D. student in the Physical Intelligence Department at the Max Planck Institute for Intelligent Systems. His research interests include mobile robotics and medical robotics.



Metin Sitti is the director of the Physical Intelligence Department at the Max Planck Institute for Intelligent Systems in Stuttgart, Germany. He was a professor at the Carnegie Mellon University, USA (2002–2014) and a research scientist at University of California at Berkeley, USA (1999–2002). He received his Ph.D. degree in electrical engineering from the University of Tokyo, Japan (1999). His research interests include physical intelligence, small-scale mobile robotics, bio-inspiration, advanced robotic materials, and miniature medical robots.

Defining magnetic gradient fields generated by the MRI gradient coils as $\vec{G}_{MRI} = [g_x \ g_y \ g_z]^T = \left[\frac{\partial B_x}{\partial x} \quad \frac{\partial B_x}{\partial y} \quad \frac{\partial B_x}{\partial z} \right]^T$, the magnetic gradient pulling force can be written as

$$\vec{F}_{gp} = VM_s \vec{G}_{MRI} \quad (5)$$

It is important to note that Equation (5) indicates that any magnetic pulling force in 3D space at \mathbb{R}^3 can be applied by an MRI device.

The MRI-driven magnetic pulling method has been widely used in the literature for various purposes, including precisely positioning magnetic beads in 3D,^[15,32,33] controlling the position of multiple capsules independently,^[26] position tracking of ferrous objects in a maze,^[32] catheter tip control,^[17,19] and building MRI-driven hammer robots for penetration into deep tissues.^[11]

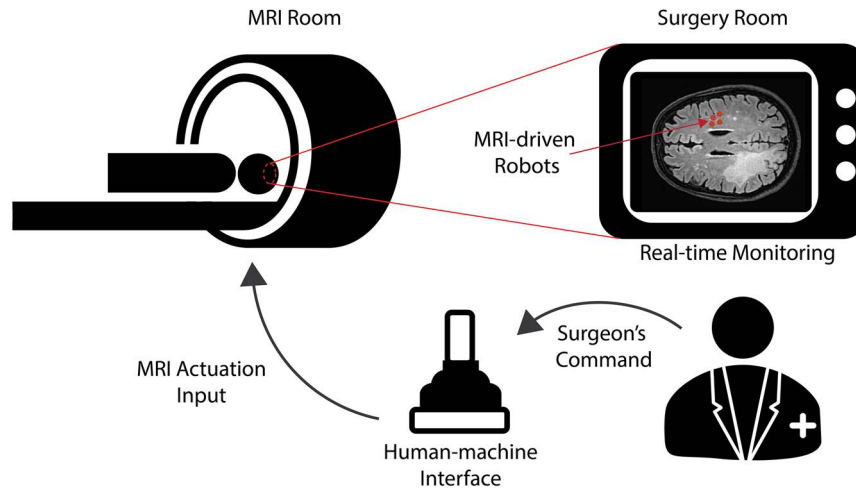


Figure 1. MRI devices can be used as wireless magnetic actuation systems for medical robots, which could convert the currently available diagnostic clinical MR scanners into theranostic medical robotic systems.

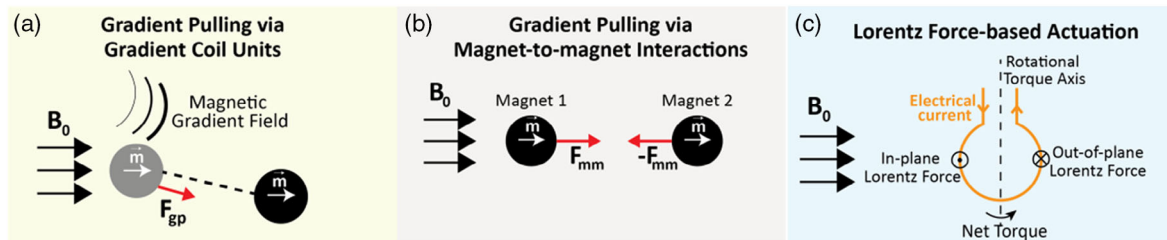


Figure 2. A pictorial depiction of three MRI-driven actuation methodologies. a) Magnetic gradient field generated by an MRI gradient coil unit creates a magnetic pulling force on a magnetic object inside MRI devices. b) Magnetic objects in MRI devices can create local magnetic gradients around them. Such local fields attract or repel other magnetic objects around them. c) A current-carrying wire under a constant strong magnetic field (e.g., under \vec{B}_0) experiences a Lorentz force on itself. Such an actuation methodology can be used to apply forces and torques on robots by powering current loops electrically inside MRI devices.

2.1.2. Gradient Pulling via Magnet-to-Magnet Interactions

Another type of magnetic gradient pulling method in MRI devices is to utilize a strong magnetic gradient field created around another a ferrous robot body. The magnetic field generated around a ferromagnetic core, \vec{B}_{core} , can be given as

$$\vec{B}_{\text{core}} = V \frac{\mu_0}{4\pi} \left[\frac{3(\vec{M} \cdot \vec{r})\vec{r}}{r^5} - \frac{\vec{M}}{r^3} \right] \quad (6)$$

where \vec{r} is the distance vector from the center of any ferrous body to any point outside of the core in 3D space. $\mu_0 = 4\pi \times 10^{-7} \text{H m}^{-1}$ is the vacuum permeability, and r is the length of \vec{r} . By inserting Equation (2) into Equation (6), the field distribution around the core in the Cartesian coordinates becomes

$$\vec{B}_{\text{core}} = VM_s \frac{\mu_0}{4\pi r^5} [3xz\vec{\hat{x}} + 3yz\vec{\hat{y}} + (3z^2 - r^2)\vec{\hat{z}}] \quad (7)$$

Under the magnetic conditions specific for MRI devices, the magnetic pulling force on a ferrous body due to another ferrous object within MRI, \vec{F}_{mm} , can be represented as

$$\vec{F}_{\text{mm}} = VM_s \vec{G}_{\text{MM}} \quad (8)$$

where \vec{G}_{MM} is the magnetic field gradient vector at any given point due to a ferrous body magnetized under \vec{B}_0 . \vec{G}_{MM} can be further derived as

$$\vec{G}_{\text{MM}} = \left[\frac{\partial B_{\text{core}_z}}{\partial x} \quad \frac{\partial B_{\text{core}_z}}{\partial y} \quad \frac{\partial B_{\text{core}_z}}{\partial z} \right] = \frac{3\mu_0}{4\pi r^7} [x(r^2 - 5z^2) \quad y(r^2 - 5z^2) \quad z(3r^2 - 5z^2)] \quad (9)$$

The representative distribution of this magnetic field gradient vector is shown in **Figure 2**. Inserting Equation (9) into Equation (8) yields the magnet-to-magnet force vector, \vec{F}_{mm} , as

$$\vec{F}_{\text{mm}} = VM_s \frac{3\mu_0}{4\pi r^7} [x(r^2 - 5z^2) \quad y(r^2 - 5z^2) \quad z(3r^2 - 5z^2)] \quad (10)$$

In proximity of a ferrous object, the magnetic gradient field strengths can be much higher compared to the magnetic gradient fields generated by MRI devices. Therefore, such a method has the advantage of generating stronger forces. It is important to note that the magnetic pulling force exerted on the target objects is highly dependent on the position of the puller magnet, and such magnetic pulling forces around the puller magnets cannot be turned off.

An MRI-driven Gauss gun utilizes the magnet-to-magnet pulling-based actuation technique to store a large potential energy for aiming and shooting a needle to penetrate tissues.^[6] The magnet-to-magnet attraction is also used for dipole field navigation in MRI scanners. Dipole field navigation aims to navigate magnetic microparticles inside MRI with a stationary large magnet set located around the bifurcations. The local interactions between such a stationary magnet set and the microparticles facilitate their navigation in microchannels in an MRI device.^[20,34,35]

2.2. Lorentz Force-Based Actuation

The Lorentz law states that moving electrons under magnetic fields experience a force perpendicular to the direction of velocity and the magnetic field. This law is given as

$$\vec{F} = q(\vec{E} + \vec{v} \times \vec{B}) \quad (11)$$

where q is the electric charge, \vec{v} is the instantaneous velocity, and \vec{E} and \vec{B} are the electric and magnetic fields, respectively. Based on this phenomenon, a current-carrying stationary wire under a magnetic field experiences a macroscopic force. Such a Lorentz force vector, \vec{F}_{Lorentz} , on a current-carrying wire can be given as

$$\vec{F}_{\text{Lorentz}} = I \int d\vec{\ell} \times \vec{B} \quad (12)$$

where I is the current flow, $d\vec{\ell}$ is the infinitesimal wire length, and \vec{B} is the magnetic field vector present on the wire. Equation (12) indicates that the stronger the magnetic field is, the stronger the forces are. Equation (12) also indicates that for a closed loop of wire, there will be a torque induced on the loop. For a coil with multiwindings, the Lorentz torque, $\vec{\tau}_{\text{Lorentz}}$, can be represented as

$$\vec{\tau}_{\text{Lorentz}} = IN(\vec{A} \times \vec{B}) \quad (13)$$

where N is the total number of windings and \vec{A} is the area plane vector of the loops.

Since \vec{F}_{Lorentz} and $\vec{\tau}_{\text{Lorentz}}$ scale linearly with the magnetic field, as given in Equation (12) and (13), utilizing such forces and torques under the strong magnetic field of MRI devices is a promising actuation methodology. Lorentz force-based actuation has been used in the literature for MRI-driven catheters^[24,25] and propulsion of MRI-driven swimming robots.^[10,36]

2.3. Comparison between Gradient Pulling-Based and Lorentz Force-Based Actuation Methods

Both the gradient pulling-based and Lorentz force/torque-based actuation methods have their advantages and disadvantages. The most remarkable advantage of gradient pulling-based actuation is the remote powering of untethered robots, which can reduce the size of the robots significantly and which allows a much larger range of navigation capabilities with no tether. In contrast, pulling such ferrous objects using an MRI scanner's gradient coils, which are also used for MR imaging, brings additional complexity in scheduling the MRI system components. It requires additional software-level and imaging sequence-level

modifications. Moreover, because each ferrous object creates a large distortion on the MR images, it is not possible to acquire the tissue image surrounding the robot. Such large distortions can be advantageous for micro- and nanoparticle imaging since they allow the detection of particles with much smaller sizes than the resolution of the MRI device.

The Lorentz force/torque-based actuation method utilizes the strong main magnetic field of MRI. Such a strong magnetic field allows exerting larger forces at any scale compared to magnetic pulling forces created by the gradient coil units of an MRI device. In addition, since a current-carrying coil induces a torque on the body, this method is more suitable for torque-based motions such as rotation and spinning. However, this approach typically requires the robot to be tethered to an external power source. Moreover, the coils may heat up significantly due to the power required for actuation and the excitation pulses of MR imaging. Therefore, the heating concerns should be considered carefully. Furthermore, this actuation method cannot exert any force and torque along \vec{B}_0 direction as Equation (12) and (13) indicate. Such a lack of force and torque along a specific direction results in singularities for this actuation strategy.

3. Localization and Tracking with MRI

3.1. MR Image-Based Localization and Tracking of MRI-Driven Robots

A typical MR imaging sequence has three fundamental stages: 1) spatial slice selection with MRI gradient coils, 2) radiofrequency (RF) excitation of protons, and 3) calculation of the inverse 2D Fourier transform of the acquired and phase-encoded signals picked up by RF receiver coils. The end product of an MR scan is a contrast-based image, whose pixel values typically are a measure of the density of MR active molecules, such as water, in the corresponding region. 2D MR images are used in two different ways to track robots in the human body: the positive and negative contrast methods.

The positive contrast method relies on detecting an outlier high-intensity signal around the robot's position. This high-intensity signal can be classified as passive, semiactive, or active positive contrast methods. The passive positive contrast methods use contrast agents such as ^{19}F , ^{13}C , and ^{29}Si as the source of the high-intensity signal.^[37–39] Figure 3a shows 2D overlaid ^1H and ^{29}Si in vivo anatomical images of mouse intestines with hyperpolarized ^{29}Si particles attached to the tip of the catheter as a passive contrast agent. The anatomy is imaged using the RARE sequence, and the hyperpolarized ^{29}Si is imaged by FLASH and RARE sequences. Alternatively, the active positive contrast methods use wire or coil antennas, which can be controlled actively to turn the contrast signal on and off, as the source of the high-intensity signal.^[40–44] An example of the active positive contrast method is shown in Figure 3b, in which a wire antenna is attached to the catheter body. During the imaging, the wire antenna is activated to increase the signal in close proximity of the catheter. The semiactive positive contrast tracking methods are based on wireless resonators, which are designed to resonate with the MRI's excitation RF field to intensify the signal created by them.^[45–53] Figure 3c shows an example of a wireless

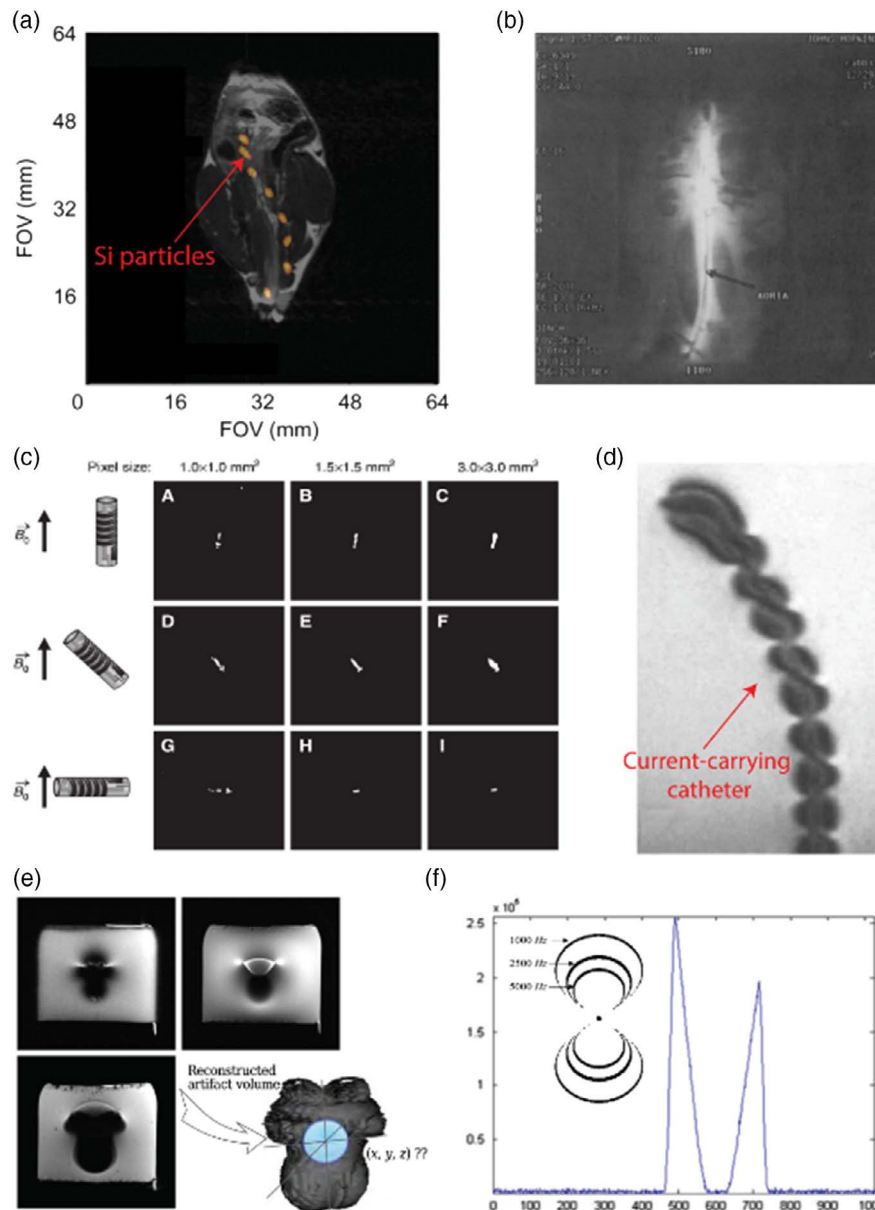


Figure 3. Imaging and localization using MRI devices. a) Overlapped image of ^1H image and ^{29}Si image; the red region is the hyperpolarized ^{29}Si particles attached on the tip of the catheter.^[39] b) Catheter antenna image without sensitivity correction, where the antenna boosts the signal around the catheter.^[40] c) Aerosol deposited MRI marker image at different angles and voxel sizes.^[45] d) The artifact image of a current-passing catheter imaged with gradient echo.^[55] e) Artifact images of a 2.5 mm magnetic bead captured by FLASH and HASTE imaging sequences and reconstructed 3D artifact shape.^[16] f) Larmor frequency shifting profile of a magnetic bead and the corresponding 1D projection image.^[58] Panel (a): Reproduced under terms of the CC-BY licence.^[39] Copyright 2015. The Authors, published by Springer Nature. Panel (b): Adapted with permission.^[40] Copyright 1997, Wiley. Panel (c): Adapted with permission.^[45] Copyright 2015, De Gruyter. Panel (d): Adapted with permission.^[55] Copyright 1997, Wiley. Panel (e): Adapted with permission.^[16] Copyright 2011, IEEE. Panel (f): Adapted with permission.^[58] Copyright 2007, IEEE.

resonator imaged by a fast field echo (FFE) sequence. These three methods result in a bright spot on MR images. The precise tracking results of such a bright spot can be overlaid on previously taken detailed MR images for a better visualization of the robot state with respect to the physiological environment.

Contrary to the positive contrast methods, the negative contrast methods utilize the absence of MR signal at specific positions to track objects. Negative contrast in MR images is

generally obtained by using non-MR active or magnetic materials attached to the robot. Non-MR active particles do not create any MR signal. Therefore, their silhouette is seen as a void in the MR images.^[54] In contrast, magnetic particles not only form a void with their shape in the image due to the lack of signal, but they also create image artifacts as in Figure 3e by distorting the magnetic field around them, which alters the Larmor frequency of close-proximity protons. It has been reported that the image

distortion around a steel bead is roughly 20 times larger than the size of the bead itself.^[20] Figure 3d shows that similar image distortions are created by passing DC currents through catheter coils, which can also be used for catheter tracking.^[55,56]

The image artifact-based negative contrast method attracts attention since the distortion provides position information for MRI-driven magnetic microrobots. The smallest navigable microrobot within MRI has been reported as a 15 μm microsphere under gradient-echo scans.^[57] Even though the robot size is much smaller than the resolution of the MRI device, the distortion size can be around the resolution of the MRI device used (reported as 500 μm \times 500 μm pixel size).

Folio et al. used image artifact-based position tracking using 2D images to obtain 3D position tracking and localization.^[16] They reconstructed the image artifacts for a steel sphere with radius ranging from 0.7 to 3.0 mm and created a stack of artifact slice templates. They run a template stack matching algorithm on images collected with standard FLASH and HASTE sequences to calculate the correlation matrix for all of the templates in the stack. The most correlated slice gives the out-of-plane distance of the robot to the slice of the image. Later, Dahmen et al. demonstrated that the template stack matching method can be performed faster by *k*-space reduction.^[32]

3.2. MR Projection-Based Localization and Tracking of MRI-Driven Robots

Acquisition of 2D or 3D MR images can provide robot position data as well as human understandable visual data. However, obtaining such rich information content brings data acquisition and computational overheads to the localization and tracking system, which deteriorate controller performance by decreasing the feedback rate. In contrast, for robotic control and manipulation, 1D line scans could provide sufficient information for localization and tracking in some cases.

Martel and coworkers developed magnetic signature selective excitation tracking (MS-SET), which acquires three projection images of the robot via a spin-echo sequence with nonselective RF excitation.^[58] Rather than slice selection by applying a magnetic gradient, this technique uses a magnetic particle embedded in the robot body, which enables an RF signal to selectively excite the protons at a fixed distance from the robot, as shown in Figure 3f. Thereby, it is possible to pinpoint the robot position in 3D space. This method provides high-frequency tracking data, but the projection scans do not produce visually meaningful images about the surroundings of the robot. Therefore, an auxiliary method is required to localize the robot with respect to the obstacles in the human body.

4. MRI-Driven Robots for Medical Applications

The imaging modality of an MR scanner combined with MRI-driven actuation and powering systems enables a single MRI system to be used for therapeutic operations combined with MRI monitoring. The advantage of such an innovative use of MRI devices is having no need for an additional imaging or actuation system unlike many other custom electromagnetic

systems.^[27,59–61] Therefore, MRI-driven robotics will be much easier to adopt for use in clinics in the near future.

The must-have properties of MRI-driven magnetic robots include being localizable, powered by MRI devices, and equipped for the requirements of the target medical task. Therefore, for medical functionality and effective design, MRI-driven robotic systems should seek to address the optimum combination of the MRI-actuation method, size, functional mechanism design, and trackability and localizability methods with MR imaging.

4.1. Robot Design

The magnetic environment inside an MRI device should be taken into consideration when designing MRI-driven magnetic robots. MRI devices have a strong \vec{B}_0 magnetic field that is present at all times and cannot be turned off or alternated. Due to such a magnetic field constraint inside an MRI device, conventional magnetic untethered robot designs that rely on temporal change of magnetic fields, i.e., those with a nonuniform magnetization profile, cannot be used in MRI devices. Therefore, locomotion and functionalities based on rotation, spinning, and undulation types of motions cannot be realized through magnetic robots inside MRI devices.^[27–30,59,62–68] In addition, the very high constant \vec{B}_0 magnetic field of an MRI device (e.g., 7 T) is typically strong enough to saturate the magnetic objects inside the bore. This field strength does not allow any complex magnetization profile inside the MRI since the magnetization profile of the robot is always aligned or magnetized along \vec{B}_0 . Ferromagnetic objects keep their magnetization when there is no strong magnetic field applied, whereas paramagnetic objects' magnetization depends on the presence of an external magnetic field. Since \vec{B}_0 is always present and very high, there is no difference in behavior of paramagnetic and ferromagnetic objects in terms of magnetic actuation inside MRI systems. The major difference may stem from the saturation magnetization strength between paramagnetic and ferromagnetic particles under such a magnetic field. Typically, paramagnetic materials are much weaker; therefore, larger volumes of paramagnetic particles would be needed to create the same magnetic force with the ferromagnetic material counterpart for any given robot.

For magnetic gradient pulling and magnet-to-magnet pulling medical devices, spherical ferrous objects are chosen because of their axisymmetric shape and directional independence of spheres under the \vec{B}_0 of the MRI device. These spheres are usually inserted in a nonmagnetic cavity or a tunnel for transferring the force but not locking the orientation.^[5,6,11,14,17,69] For Lorentz torque-based actuation methods, typically the Lorentz coil is firmly attached to a flexible body to induce a local torque where it is located. Such a torque is used to deform the flexible body to control a catheter tip orientation^[25,70] or create a propulsion force in a fluid.^[10,36]

4.2. Medical Device Types

MRI-driven medical devices can be segmented into two main categories based on their scheme of usage: untethered and tethered devices. Untethered devices such as magnetic microrobots are not fixed and can freely move around within the confinements of the body, typically guided by smart control algorithms such

as proportion-integral-derivative (PID) control. Tethered devices such as catheters remain attached or fixed to the user as they insert the device into the patient. Both types of devices have been driven in the MRI systems by using the aforementioned MRI-actuation approaches. **Table 1** and **2** summarize the MRI-driven medical device studies in the literature with selected key aspects for medical use.

4.2.1. Untethered MRI-Driven Robots

The actuation and control of untethered MRI-driven magnetic robots rely on magnetic pulling forces. Such forces can be generated either by the MRI device itself or by interaction with another ferrous object in proximity of the robot. Using MRI-driven untethered devices, which consist of such ferrous objects

Table 1. Properties of MRI-driven untethered medical robots in the literature.

Article	Actuation method	Actuator dimension (diameter)	Overall dimensions	Overall shape	Materials	Imaging modality	MRI sequence	MRI duration	Actuation duration	Feedback rate	Motion DoF	Motion precision	Control method	Application
[14,69]	Gradient Pulling	1 mm	80 × 50 × 50 mm ³	Axisymmetric rod-like assembly	NdFeB magnet and 3D-printed compartments	Camera	N/A	N/A	N/A	10 Hz	5	0.2 mm in height and 0.02 rad in orientation	Closed-loop PID control	Navigation
[11]	Gradient Pulling	2–6 mm	50 × 7 × 7 mm ³	Hollow tube with a sharp needle tip	Stainless steel and plastic container	Camera and microphone	N/A	N/A	Continuous	N/A	1	N/A	Partially closed loop control	Tissue penetration
[16,32]	Gradient Pulling	0.75–3 mm	0.75–3 mm in diameter	Sphere	Steel	MRI	Optimized FLASH and HASTE	960 ms	500 ms	0.33 Hz	2	0.31 mm	Closed-loop PID controller	Navigation
[20,34,35]	Gradient Pulling and Magnet to Magnet Interactions	38.1 mm	38.1 mm in diameter	Sphere	Chrome steel	Camera and MRI	Spin echo and turbo spin echo	N/A	Continuous	N/A	2	N/A	Open-loop control	Navigation
[15]	Gradient Pulling	2.34 mm	2.3 mm in diameter	Sphere	Chrome steel	MRI	Modified 1D spin echo	5.5 ms	3.4 ms	112 Hz	2	N/A	Event-based control with waypoints	Navigation
[6]	Gradient pulling and magnet to magnet interaction	6 mm	30 × 30 × 10 mm ³	Rectangular modular boats	Chrome-steel	MRI	Projection-based spin echo	>20 ms	N/A	N/A	2	N/A	Open-loop control	Tissue penetration
[13]	Gradient Pulling	1 mm	1 mm in diameter	Sphere	Chrome steel	Camera	N/A	N/A	N/A	N/A	3	N/A	N/A	Navigation
[7,8]	Gradient Pulling	6 mm	100 × 100 × 60 mm ³	Rectangular assembly with sphere actuator	LEGO plastic/ chrome steel	MRI	Single-dimension gradient echo	12 ms	5000 ms	0.19 Hz	3	0.65 mm	Closed-loop PID control with state estimator	Needle insertion and biopsy
[26]	Gradient Pulling	1–1.5 mm	3–6 mm in diameter	Sphere	Chrome steel	Camera	N/A	N/A	N/A	N/A	2	4–6 mm	Open-loop control	Multirobot navigation
[22,23]	Gradient Pulling	206 nm	0.053 mm in diameter	Spherical particle	FeCo nanoparticles with cancer drug	MRI	Coronal T2*-weighted gradient echo	N/A	Continuous	N/A	1	N/A	Open-loop control	Navigation
[18]	Gradient Pulling	4.75 mm	84.75 × 10 × 4.75 mm ³	Sphere ball connected to an 80 mm long tail	Carbon-steel alloy and thin-acetate sheet	Camera	N/A	N/A	Continuous	N/A	2	N/A	Open-loop control	Navigation
[21]	Gradient Pulling	0.011 mm	0.65 mm in diameter	Particle aggregate—random shape	Fe ₃ O ₄	Camera	N/A	N/A	Continuous	N/A	1	N/A	Open-loop control	Navigation
[79]	Gradient Pulling	1.5 mm	1.5 mm in diameter	Sphere	Chrome steel	MRI	Gradient echo MS-SET	22 ms	8–17 ms	25–32 Hz	2	N/A	Closed-loop PID control	Navigation
[4,94]	Gradient Pulling	3.175 mm	3.175 mm in diameter	Sphere	Carbon steel	MRI	Fast gradient echo	N/A	10 ms	N/A	2–3	N/A	Open-loop control	Navigation

Table 2. Properties of MRI-driven tethered medical robots in the literature. SSFP, steady-state free precession.

Article	Actuation method	Catheter diameter [mm]	Overall dimensions	Overall shape	Imaging modality	MRI sequence	MRI duration [ms]	Motion DoF	Motion precision [mm]
[70,74]	Lorentz torque	3.2	3.8 mm in diameter	Catheter tube	MRI and camera	N/A	N/A	2	3–5
[75]	Lorentz torque	3.18	N/A	Catheter tube	Camera	N/A	N/A	2	13.5
[72]	Lorentz torque	0.9	1.6 mm in diameter	Catheter tube	MRI and X-ray	Single-section balanced SSFP	434	2	N/A
[95]	Lorentz torque	1.2	2 mm	Catheter tube	MRI and camera	Balanced SSFP (FIESTA)	N/A	1	N/A
[10,36]	Lorentz torque	N/A	12 × 12 × 32 mm ³	Spheroid with three tails	MRI and camera	2D spin echo and gradient echo	500	3	N/A
[17,19]	Gradient pulling	1.5	2.1 mm in diameter	Catheter tube	MRI and camera	TurboFLASH and MS-SET	N/A	2	N/A
[77]	Gradient pulling	2.6	2.6 mm in diameter	Catheter tube	MRI	2D FLASH	350	2	1–4
[25]	Lorentz torque	0.6	0.75 mm in diameter	Catheter tube	MRI	Balanced SSFP (FIESTA)	N/A	1	N/A
[24]	Lorentz torque	0.75	1.3 mm in diameter	Catheter tube	MRI	2D FLASH sequence	30	3	N/A
[73]	Lorentz torque	0.77–0.9	2 mm in diameter	Catheter tube	MRI	SSFP	330–500	1	N/A
[2]	Lorentz torque	0.77–1	2 mm in diameter	Catheter tube	MRI	SSFP	200–500	2	N/A

as the powering unit, enables the ability to move them around in the human body with magnetic pulling forces. Such devices can be utilized for medical applications in which navigation is very challenging, or for more efficient surgical procedures in medical interventions. Studies on untethered MRI-driven robots are classified according to their navigation and intervention capabilities based on their target medical use. Such a classification of untethered MRI-driven robots and some examples from the literature are presented in **Figure 4**.

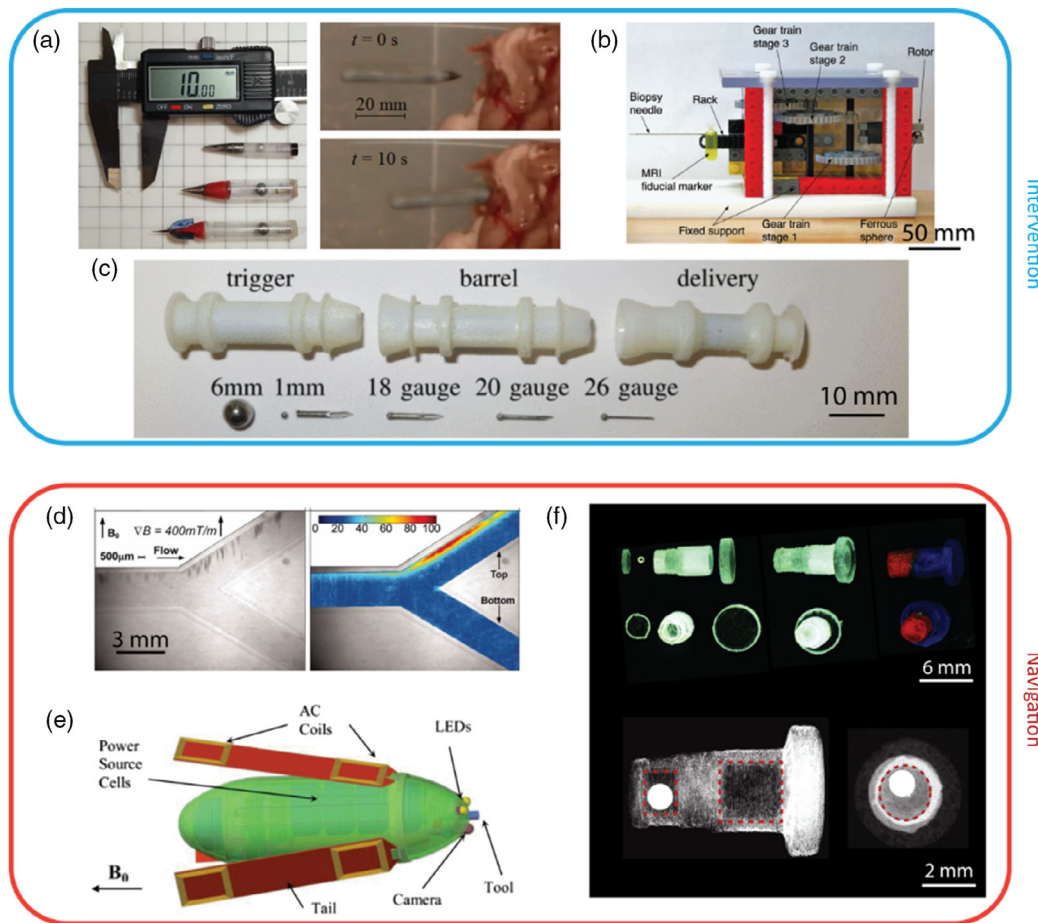
Navigation: Martel et al. navigated a 1.5 mm diameter ferromagnetic bead in a carotid artery of a living swine using MRI devices.^[33] The navigation of the bead is achieved via magnetic gradient fields generated by MRI devices. Mathieu and Martel have shown that MRI devices are capable of steering aggregated magnetic microparticles in flow conditions (Figure 4d).^[21] This study focuses on gradient pulling–based actuation with MRI devices. These particles are also tracked with the same MRI device. A y-shaped channel with a constant fluid flow is used as a representative bifurcation setup. To provide strong gradient pulling forces, an additional gradient coil insert is designed and used during the experiments. This gradient coil insert can generate 400 mT m⁻¹ gradients. This study has been further improved upon by Michaud et al. to investigate the performance of this application under realistic medical environments.^[71] In this study, animal experiments are conducted to acquire clinically relevant physical conditions in pig arteries. The results are used to emulate such a flow environment for in vitro experiments to analyze the success of an embolization operation. A glass embolization channel with a smooth inner surface is used for demonstration. The study provides promising results for embolization; however, this study should be investigated further for in vivo applications, where vessel geometry and features may alter these results together with the pulsatile blood flow.

Kosa et al.^[10] presented a swimming technique that relies on creating local deformations on a soft tail attached to a pill-sized swimming robot.^[36] The local deformations are created by the Lorentz torque–based actuation methodology. The Lorentz torque is generated by a current-carrying coil that is located on the swimming tail of the robot. These coils are tethered and powered by an external electrical energy source. The electrical current

magnitude and direction on these coils determine the local torque, and thus the deformation on the robot's tail. They have shown characterization and testing of such deformations and the resultant propulsion forces on the tails in a 3 T MRI scanner. It is reported that a 20 mm long by 5 mm wide swimming tail produces 0.21 mN propulsive force on average with a 20 Hz signal (Figure 4e). This study shows deformation of a single tail only; a complete robot actuation under an MRI device has not been demonstrated.

Erin et al. designed an untethered magnetic robot that can perform not only position steering but also orientation steering in 3D stagnant fluids under constant magnetic fields similar to those in MRI devices.^[14,69] The robot consists of a ferrous bead and nonmagnetic component body parts. The ferrous bead, which is free to rotate inside the millirobot and located away from the center of mass, facilitates the generation of not only net forces but also induced torques with the applied magnetic field gradients. This force and torque couple on the robot leads to translation and rotation of the robot simultaneously under the presence of a constant and strong \vec{B}_0 field. This method focuses on the fix-orientation challenge of MRI-driven untethered miniature robots and shows the robot orientation is controllable via MRI gradient pulling. Such a design approach allows MRI-driven untethered robots to accomplish orientation-dependent tasks, such as conducting biopsy and camera and laser steering, despite the static and strong \vec{B}_0 field (Figure 4f). Although these studies show the orientation control of an MRI-driven untethered robot, simultaneous control of both the position and orientation of such robots still remains a challenge.

Latulippe and Martel anchored puller magnets 12.7 mm in diameter at predefined locations for guiding magnetic microparticles in bifurcations.^[34,35] The puller magnets were used to steer microparticles at bifurcations by employing the local magnetic pulling forces generated around the carbon-steel core. This core can create magnetic gradient fields exceeding 300 mT m⁻¹ on the microparticles and attracts these particles toward desired channels. Although the advantage of such an approach is the capability of creating large pulling forces, the study does not show reprogramming of the desired steering paths on the fly for any other steering directions in complex channels. Such



Intervention

Navigation

Figure 4. Examples of untethered MRI-driven medical robots in the literature. a) MRI hammer to penetrate deep in soft tissues.^[11] b) MRI-driven biopsy needle.^[8] c) MRI-driven Gauss gun for deep tissue penetration.^[6] d) The steering of magnetic microparticles via magnetic gradient pulling inside an MRI device.^[21] To provide stronger forces, an additional MRI gradient coil insert unit has been used to steer the microparticles. This method has been demonstrated to be used for embolization with magnetic microparticles in MRI devices.^[71] e) Conceptual depiction of an MRI-driven swimmer.^[36] f) A rotatable magnetic robot that can achieve both position and orientation control under constant magnetic fields of an MRI device and actuated by magnetic gradient pulling.^[14,69] Panel (a): Adapted with permission.^[11] Copyright 2017, IEEE. Panel (b): Adapted with permission.^[8] Copyright 2013, Wiley. Panel (c): Adapted with permission.^[6] Copyright 2015, IEEE. Panel (d): Adapted with permission.^[21] Copyright 2010, IEEE. Panel (e): Adapted with permission.^[36] Copyright 2015, IEEE. Panel (f): Adapted with permission.^[69] Copyright 2019, IEEE.

reprogrammability may require controlling multiple puller magnets individually and bringing them to any desired location.

Intervention: Leclerc et al. have shown the design principle of hammer-like MRI-driven robots for tissue penetration.^[11] The robot is actuated by a ferrous sphere, which is located inside a hollow tunnel. With an oscillating magnetic gradient pulling force, the bead is pushed and pulled back and forth inside the tunnel, creating an impact penetration force, like a hammer, inside the tissue. Penetration of the hammer-like robot in a sheep brain is performed to demonstrate brain interventions toward medical applications (Figure 4a). This approach works best for lateral penetration; however, any penetration direction that has a negative or positive slope (i.e., direction component along the gravity axis) results in a reduction in the penetration performance of such a robot.

Vartholomeos et al. have designed a needle biopsy device that is powered by MRI's magnetic gradient fields.^[8] The device is grounded inside the MRI next to the target tissue. A 2.5 mm

diameter ferrous bead is used to actuate the designed gear train that precisely moves and positions the needle tip. The swine heart biopsy trial with a 21-gauge bevel tip biopsy needle is shown with 20 and 40 mT m⁻¹ gradient field strengths (Figure 4b).

Becker et al. demonstrated an MRI-driven Gauss gun device that can create strong impact forces to penetrate a needle tip in deep tissues.^[6] The Gauss gun consists of multiple units: a trigger, a barrel, and delivery. Each unit consists of a 6 mm diameter alloy steel sphere and a plastic rod to transfer the moment from one unit to another. The delivery unit has an additional needle tip for delivery to penetrate in tissues. The trigger unit activates the needle shot as soon as the magnet-to-magnet interaction exceeds a threshold distance, at which the stored magnetic potential energy is converted into kinetic energy. These components are navigated via magnetic gradient pulling forces generated by MRI devices, while the needle-shot is activated by magnet-to-magnet interactions (Figure 4c). Since the actuation/triggering mechanism relies on magnet-to-magnet attraction between each unit,

such an attraction force can only be created along the direction of the bore (\vec{B}_0). Therefore, this biopsy needle can penetrate tissues only along the direction of the bore (\vec{B}_0).

4.2.2. Tethered MRI-Driven Robots

The use of catheters in the surgical setting is a standard and well-known practice in the medical field. Navigation and control of such catheters is critical for many different medical applications. MRI-driven catheters utilize either the strength of the uniform magnetic field or the applied magnetic field gradients to bend the catheter shape. Catheter tip control via Lorentz force/torque is an advantageous actuation technique since MRI devices already have a very strong magnetic field. For Lorentz torque-based actuation methods, typically the Lorentz coil is firmly attached to a flexible body to induce a local torque where it is located. Such a given torque is used to deform the flexible body to control the catheter tip orientation.^[25,70] In terms of catheter coil design, generally one or more sets of coils, referred to as “saddle” or “axial” depending upon the design, are wound,^[24,25,70] 3D-printed,^[46] or cut using laser lithography at the tip of the catheter.^[2,72] A Lorentz torque is generated on the tip when current flows through these coils, allowing direct user control of the catheter tip.

Roberts et al. made a three-axis coil wound on a 1.5 F catheter demonstrating the feasibility of MRI-driven catheter deflection.^[24] Settecasse et al. also designed a 1.8 and 5 F catheter actuated by Lorentz torque under 1.5 and 3 T MRI devices.^[25] Wilson et al. improved the design by manufacturing microcoils using a novel laser lithography approach on 2.3–3.0 F catheters.^[2] However, these designs did not address coil heating, which could cause damage to the surrounding tissue. This issue was resolved later by Hetts et al. by regulating the current to less than 300 mA with less than 1 min activation times and using a saline coolant

under a 1.5 T MR scanner.^[73] Liu et al. developed and validated a 3D kinematic model and control of 3 F MRI-steerable catheters within 3 T MR scanners designed specifically for accessing the workspace of the heart for atrial fibrillation.^[70,74,75] This model was later improved with a design optimization of an MRI-driven catheter given more than one coil set.^[76]

Catheters have also been steered utilizing the gradient coils of an MRI. In these studies, the magnetic gradient field generated inside of an MRI scanner is used to exert a magnetic pulling force on the tip of the catheter, which is used to bend the catheter. Zhang et al. showed gradient pulling and localization of an intravascular catheter with a magnetic tip.^[77] Gosselin et al. also demonstrated gradient pulling on a catheter with a ferromagnetic tip consisting of one or two spheres using a custom set of gradient coils.^[17,19] Their results showed that increasing the number of ferromagnetic spheres increases the deflection of the catheter but introduces dipole–dipole interactions as well as larger image artifacts. Some of the selected studies on tethered MRI-driven robots are shown in **Figure 5**.

5. System Structure of MRI-Driven Robotics

MRI devices consist of a combination of highly precise hardware and software systems that interprets data generated from the precession motion of proton atoms. In terms of hardware, typical MRI devices consist of three major types of coil sets: 1) a super-cooled electromagnetic coil (main magnet), 2) three sets of gradient coils, and 3) transmitter and receiver RF coils for excitation of and listening to the protons. The atom precession is of the orders of tens or hundreds of megahertz. The RF excitation pulses and magnetic gradient switching occur at nanosecond resolution. To have a successful imaging with such sensitive and

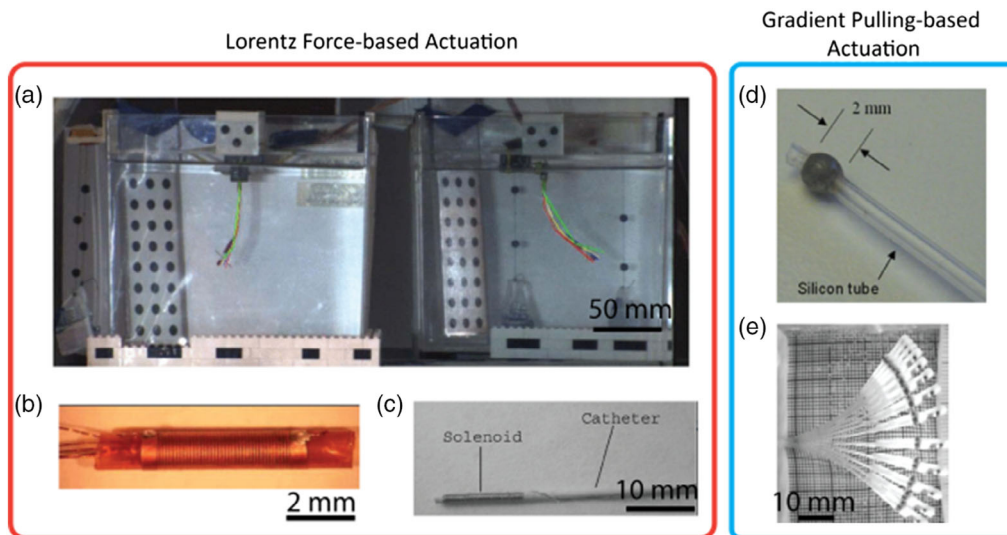


Figure 5. Examples of MRI-driven robots actuated by the Lorentz forces in the literature. a–c) MRI-driven catheters with Lorentz coil embedded.^[2,25,75] The torque induced on an active Lorentz coil deforms the tip, which enables precise tip control within MRI. d,e) MRI-driven magnetic gradient pulling-based catheter designs.^[19,77] The ferrous tip can exert magnetic pulling force with spatial magnetic field perturbations of the MRI device. This exerted force can bend the catheter tip and provides control of these devices. Panel (a): Adapted with permission.^[75] Copyright 2017, IEEE. Panel (b): Adapted with permission.^[2] Copyright 2013, Elsevier. Panel (c): Adapted with permission.^[25] Copyright 2007, Wiley. Panel (d): Adapted with permission.^[77] Copyright 2010, Springer Nature. Panel (e): Adapted with permission.^[19] Copyright 2010, IEEE.

fast MR physics of the protons, the electromagnets are built with very high precision and controlled with high temporal resolution. In addition to the precise manufacturing and control of the hardware, timing of the control of the hardware should be very precise. Therefore, communication delays and control rates between the software and hardware have to be very reliable with minimum amount of deviation from their nominal durations. In short, MRI devices are highly engineered, interdisciplinary devices that are widely used in clinics for diagnosis.

Depending on the actuation technique utilized, the system level evaluation and requirements of MRI-driven robotics differ. For example, having a strong magnetic field is highly advantageous for Lorentz torque-based robotic design approaches since the torque generated scales linearly with the magnetic field strength. However, this requires additional coils on the robot, which introduces more elements for MRI-driven systems. Excessive heating of the Lorentz coils become an additional concern in such a situation. Another approach for actuation is to utilize the magnetic gradient field available in MRI devices for magnetic pulling-driven robotic designs. The magnetic coil inserts are responsible for generating the gradients needed for imaging. This unit is optimized for imaging, which means linearity of gradient, a fast switching rate, and low temperature rise are the major features of these units.^[78] The typical magnetic gradient field strength is around 40 mT m^{-1} for clinical MRI devices. Even though there are many studies that use such magnetic gradient strengths for actuation of MRI-driven robots, this gradient strength may not be sufficient for some robotic applications. To overcome this issue, Martel and coworkers have designed their own propulsion gradient inserts, which can generate up to 400 mT m^{-1} , in addition to MRI gradient coil units.^[13,19,21,22] Their approach can be used to generate stronger magnetic gradient fields, and therefore, stronger magnetic pulling forces on magnetic objects inside an MRI device. However, using such hardware reduces the workspace inside the MRI bore.

The use of MRI devices differs based on the actuation technique used. From the system-level point of view, Lorentz torque-based actuation methodologies require the robot to be under the strong and constant magnetic field of an MRI device. While the powering of the Lorentz coils is achieved separately by an external coil driver, MRI devices are used for generation of high magnetic fields and for MR imaging-based monitoring and feedback. In this scheme, the scheduling of actuation and imaging cycles is only required to minimize image distortions for Lorentz torque-based devices.^[55] In contrast, magnetic gradient pulling-based actuation methods require the MRI magnetic gradient coils to be used for both imaging and actuation. The scheduling between the dual use of MRI gradient coil units introduces additional complexity into MRI-driven robotic systems. Most of the problems addressed in this section belong to the secondary actuation principle, where the magnetic gradient coil unit is used for both imaging and actuation.

5.1. Alternating Tracking and Actuation

Although it is possible to devise a custom software structure with more flexible control over the hardware, for practical reasons,

until now, researchers have preferred to use high-level communication interfaces designed by MRI device manufacturers.^[32] These communication interfaces allow the controller to set the actuation gradient for a prespecified duration at the beginning of the alternating tracking and actuation (ATA) sequences and sends the MR imaging data to the controller to be processed.

The first such ATA sequence was created by Chanu et al.^[79,80] On the MRI side of the software, the sequence starts with the propulsion phase (15 ms), and then, it follows a spin-echo-based 3D tracking sequence (15 ms).^[58] The readout signal is converted into a digital signal and processed to obtain the 3D position of the robot in the Cartesian coordinate frame. The controller calculates required magnetic field gradients to steer a robot to the desired position using the raw position data and sends this information to the MRI sequence. However, this input cannot be executed immediately, since the next ATA repetition has already started. Therefore, this technique embodies a delay of at least one ATA repetition duration, which is 30 ms.

A similar ATA sequence architecture is also used by Felfoul et al.^[7] By adding a 20 ms long second actuation phase following the imaging to the ATA sequence, Felfoul et al. created a time window for signal processing, and the actuation signal calculation for the next sequence. Furthermore, in this study a Kalman filter-based state estimator is used to provide state information during the actuation phase of the ATA sequence and to compensate for imaging noise.

5.2. Simultaneous Tracking and Actuation

Felfoul et al. demonstrated high-frequency simultaneous tracking and actuation (STA).^[15] Their approach is based on the fact that the robot position data can be acquired from MRI projection imaging in any direction in 3D space. Furthermore, they observed that position information in only certain directions is needed for basic navigation. Therefore, a simple 1D line scan can be used for imaging. Building on this idea, Felfoul et al. created a projection imaging sequence of 5.5 ms (182 Hz), which can apply 60% of the available actuation force if the magnetic gradient is applied throughout the sequence. They also mention that the minimum frequency of STA decreases to 112 Hz if one wants to achieve imaging with no propulsion by adding a minimum required spoiler gradient duration, which cancels the effect of the gradients due to imaging. They also compared the available actuation force as a function of the sequence frequency. Furthermore, in this sequence design the tracking is performed before actuation; therefore, for sequence frequencies smaller than 64 Hz it is possible to calculate the control input for the next sequence during the actuation, but for frequencies of 64–100 Hz the control signal will be delayed for one sequence and for higher frequencies the control sequence will be delayed for two sequences. They also stated that they use a Kalman filter to fuse the robot position signals achieved from two different receiver antennas and when the signals are below a threshold, they update the position based on the model only. Studies on various system structures of MRI-driven robotics are summarized in **Figure 6**.

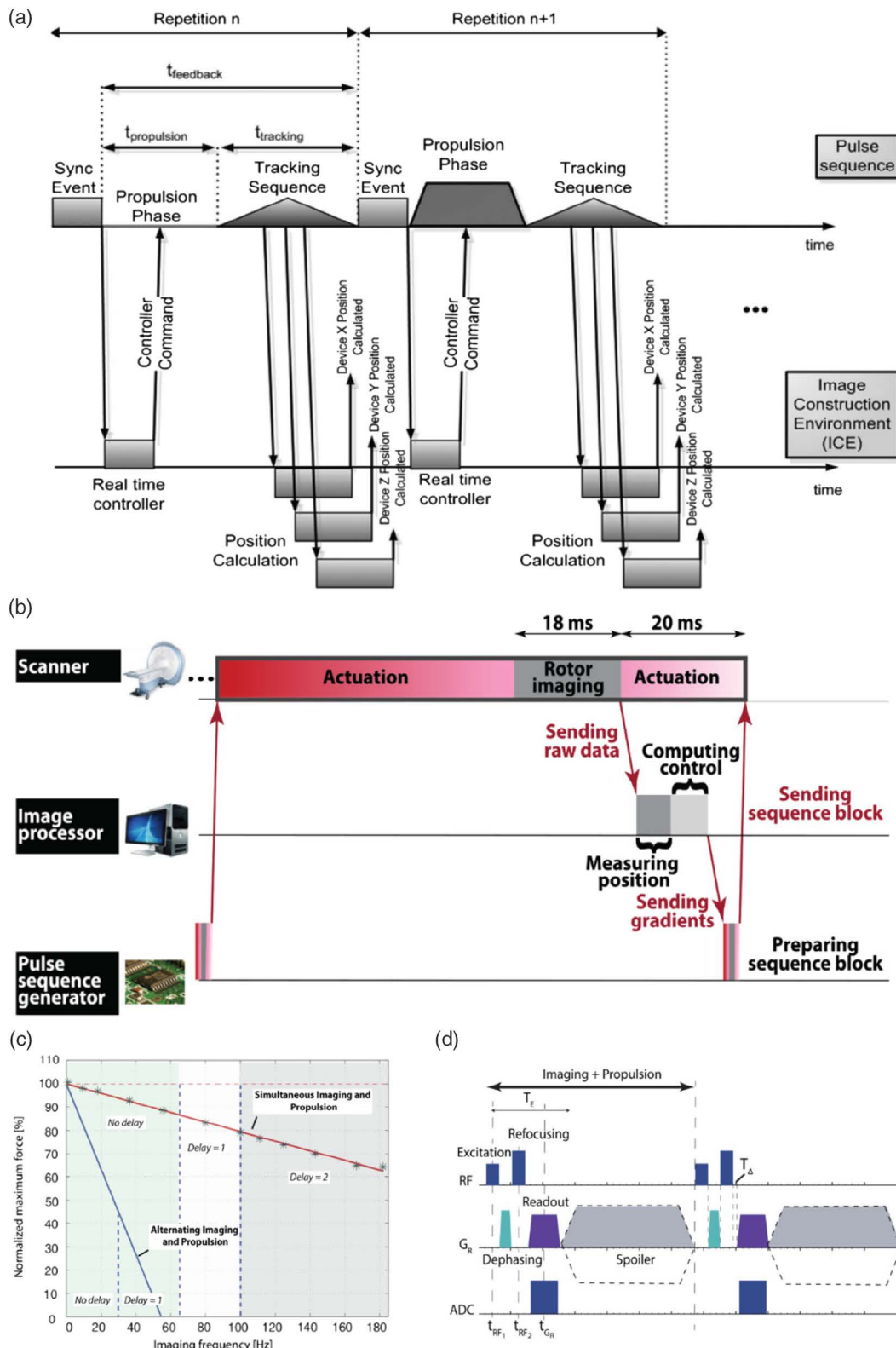


Figure 6. An overview of high-level signal structure for dual use of MRI devices for imaging and actuation. a) ATA sequence for a ferromagnetic bead.^[79] b) ATA for an MRI-driven actuator.^[7] c) Performance comparison of ATA and STA methods.^[15] d) STA sequence for a ferrous bead.^[15] Panel (a): Adapted with permission.^[79] Copyright 2008, Wiley. Panel (b): Adapted with permission.^[7] Copyright 2015, IEEE. Panels (c) and (d): Reproduced under terms of the CC-BY licence.^[15] Copyright 2016. The Authors, published by Springer Nature.

6. Safety Issues

In the development of MRI-driven medical robotic systems, safety is a critical aspect to be considered for their clinical use. The risks and effectiveness of the developed systems need to be assessed from various sides, for example, the risk of materials used, the effect of magnetic and electric fields, and the specific risks associated with particular procedures and the targeted parts of the body. There are governmental organizations issuing legally binding regulations, such as the Food and Drug Administration (FDA), European Medicines Agency (EMA), and the China Ministry of Health, and organizations issuing guidelines, such as the International Electrotechnical Commission (IEC) and the International Commission on Non-Ionizing Radiation Protection (ICNIRP), to minimize such effects for the protection of patients.^[81] There are also regulations to protect workers issued by such organizations, for example, the USA Occupational Safety and Health Act (OSHA).^[81] However, especially at the research step, it would be wise to be aware that these rules and guidelines can be open to modification/exceptions depending on the benefit and the risk. Therefore, it would be beneficial to know the underlying reasons behind these regulations and guidelines.

In MRI systems, the major safety concerns source from magnetic fields and induced electric fields and currents. These fields may cause safety issues either through their direct interaction with the human body or through affecting other materials embedded in the human body or materials used in medical operations. Here, we summarize the major safety issues related to the main magnetic field of MRI, as well as fields produced by gradient coils and RF coils, which can be found in more detail in Panych and Madore^[82] and ICNIRP.^[83,84]

6.1. Main Magnetic Field

The main (static) magnetic field of current human MRI scanners is typically 1.5 or 3 T, which are the ones mostly available in clinics, and it is possible to see even 10.5 T (which is about 200 000 times stronger than the magnetic field of earth) in preclinical environments.^[82] Such strong magnetic fields can be highly dangerous as they can exert strong forces and torques on any magnetic material coming close to MRI. The static field of MRI is rather uniform in the bore and decays with distance in general, but note that the exact profile of the magnetic field around MRI depends not only on the MRI itself but also on the surrounding materials, such as shielding structures. The static (main) magnetic field of MRI is expected to cause no net force in the bore as attraction forces are based on the gradient of the magnetic field. However, the gradient of the main field can be highly strong right outside. Moreover, there can be a strong magnetic torque on magnetic materials also in the bore even if no attraction force is expected. If these materials are embedded in the human body, any strong force or torque can be extremely dangerous. Therefore, normally, no magnetic material is allowed in MRI scans. All of these concerns should also be considered in MRI-driven robotic operations, as any undesired pulling forces and torques on magnetic robots can harm patients, if not handled properly. A method to avoid undesired attraction forces during insertion to the bore is to fix them firmly during this insertion

time. Once robots are in the bore, undesired forces are not present anymore as the main field is uniform in the bore. After this point, the operator can remove the firm attachment of the robot and insert the robot into the surgical site. After the completion of the procedure, the operator has to fix the robot again before taking the robot and the patient out to prevent postoperation damages due to the stray field. Undesired torques can be avoided by putting magnetic materials in the robot in the direction they would align under the static field of MRI. In addition to these, the forces and torques on any current-carrying wires also need to be considered when combining electronic tools with MRI systems.

6.2. Gradient Coils

Another magnetic field source in MRI is gradient coils. Gradient coils produce time-varying magnetic fields which have frequencies lower than those of the fields produced by RF coils and their strength is much lower than the main magnetic field of MRI. Undesired forces on magnetic objects due to gradient coils do not pose a high risk, but the forces formed on gradient coils due to the interaction of the electrical current and the main field of MRI cause the motion of gradient coils. High noise generated by this motion can damage the ears; thus, protection is needed during MRI scans. Another issue is the stimulation of nerves and muscles by the induced electric fields. Stimulation of peripheral nerves has been observed in patients but this does not pose a life-threatening risk. However, cardiac stimulation can be of high risk. In the current clinical systems, cardiac stimulation does not seem to be a risk, but some research systems, in theory, have the potential to stimulate cardiac tissue.^[82] The effect on metallic devices in the human body or inside MRI is also a point to consider about safety. Although the concern about electrical current induction in metallic pieces is less than in the case of RF coils, gradient coils can induce current and electronic devices should also be evaluated from the perspective of the electrical currents induced by them.

6.3. RF Coils

The magnetic fields of RF coils are applied at much higher frequencies, namely, the Larmor frequency, which is of the order of hundreds or tens of megahertz. The main concern about the field of RF coils is the heating of tissue. This can happen either directly or through some metallic materials/devices. The evaluation of safety is done from the whole-body exposure and local heating perspectives. It is reported that there is no expected adverse effect if the body core temperature is less than 1 °C, whereas this is 0.5 °C for infants and patients with cardiocirculatory impairment. It is acceptable if the localized heating in the head stays lower than 38 °C, in the trunk lower than 39 °C, and in limbs lower than 40 °C.^[84] The other important safety issue about RF coils is the heating of metallic materials. As the wavelength of the RF waves can be of the order of the sizes of those metallic materials/devices, not only magnetic but also electrical coupling needs to be considered, such as in the case of metallic rods turning into antennas. In such cases, extreme heating spots can form and harm the patient.^[82]

To translate MRI-driven medical robotic systems into clinics, a set of well-planned research and reporting stages should be completed. First of all, the principles of Good Laboratory Practice (GLP) procedures should be followed carefully with appropriate study planning, conducting, monitoring, reporting, and archiving. This is the stage where no human subjects are involved. These studies only stay at the preclinical level. As a next step, Good Clinical Practice (GCP) procedures for clinical evaluations of these robotic systems should be tested, including study details on designing, recording, and reporting experimental trials including human subjects. The evaluations of such medical robotic systems are conducted according to International Organization for Standardization (ISO) rules. ISO 10993, *Biological Evaluation of Medical Devices*, rules standardize the studies on these medical robotic devices at the in vitro and in vivo level.^[85] GLP procedures should be followed well for the assessment of ISO 10993 standards. ISO 14155, *Clinical Investigation of Medical Devices for Human Subjects*, provides sets of standards for the advanced stages of translation of MRI-driven medical devices into clinics.^[86] This stage standardizes human trials of these medical devices. The aforementioned GCP practices to assess the safety and performance of medical devices should be followed well for the assessment of ISO 14155 standards.

One of the future directions of MRI-driven robotics is to develop autonomous surgical systems to be used in clinics. Robotic assisting devices for surgeons with different levels of autonomy are the main purpose of this research direction. Depending on the level of autonomy, the regulations and ethical and legal considerations should be evaluated carefully.^[87]

7. Future Outlook and Conclusions

Converting clinical MRI devices into an actuation and imaging unit promotes MRI-driven minimally invasive surgeries with increased precision and effectiveness. For example, monitoring and controlling the navigation of MRI-driven microrobots in the human brain would reduce the operation time and increase the rate of success of critical brain surgeries that would otherwise require invasive operations on the human skull. In addition, such dual use of clinical MRI devices reduces the required hardware complexity, which takes MRI-driven robotics one step closer to being translated into clinics.

In addition to these advantages, adding new capabilities to MRI devices and MRI-driven robots introduces additional robotic complexities that are not present in typical untethered milli/microrobotic systems. MRI-driven robotics face two major challenges: 1) limited feedback rate from MRI devices for tracking and localization and 2) limited magnetic pulling forces generated via magnetic gradient coils of MRI devices. Tracking and localization data acquired by MRI systems can be around 100 Hz when simultaneous imaging and actuation sequences are used,^[15] however, it lacks the true position information since these frequencies can be achieved when only single 1D line scans are used. Typically, the feedback rates are at around 10–30 Hz for sequential actuation and tracking sequences.^[9,13,20,32] Unlike standard robotic approaches, where high-speed cameras or high-performance computers provide very accurate estimation

at much higher frequencies, the limited feedback data could be one of the challenges for medical applications under highly dynamic environments. Combining MRI devices with complementary imaging modalities, such as PET and ultrasound, could be a potential solution to the low feedback rate of MRI systems.

The magnetic gradient pulling-based actuation method has a limited gradient strength, which results in lower magnetic pulling forces on magnetic robots. Navigation against a fluid flow or operations requiring high mechanical forces/torques, such as biopsies, might not be achievable by magnetic gradient-based pulling methods. Magnet-to-magnet-based actuation methods could appear as an alternative, where strong forces can be exerted on ferrous objects that are close to each other. However, these applications usually suffer from a “single-shot” use and are limited to only a fix-direction application (along the longitudinal direction of MRI devices) for biopsy or needle penetration.^[6] A hybrid method presented by Latulippe et al. could be a useful approach to overcome the limited-force issue within MRI devices.^[20] Latulippe et al. combine magnetic gradient pulling-based actuation with magnet-to-magnet interactions to provide strong local magnetic forces, in which the puller magnet can be moved with magnetic gradient pulling, for more controlled and successful navigation of ferrous microparticles under stronger flows.

Another alternative solution to generate stronger forces in MRI without increasing the size of ferrous materials is to insert additional magnetic gradient coil hardware.^[13] Unlike the magnetic gradient coils available in MR scanners, which are optimized for linearity of the gradient field and fast switching rates of the gradient fields,^[78] such actuation gradient coil inserts are optimized for generating stronger magnetic gradient fields with effective cooling systems.

7.1. System-Level Architecture

MRI-driven robotics is in the early development stage, where the potential capabilities are yet to be discovered. An MRI-driven robotic system is composed of 1) MRI-based feedback acquisition, 2) MRI actuation and control, and 3) system-level integration and scheduling of imaging and actuation. The major directions of robotic systems are to explore the most effective system configuration that can image/sense the robot and anatomy, actuate, and control the robot. Since each of these elements is highly connected with the others, MRI-driven robotic systems should be studied as a whole to achieve the highest potential of these robots for a given medical tasks.

One important future direction is to study when/what kind of feedback information is truly needed. MRI can provide 3D, 2D, or line projection-based information. Answering when and which one of this information is required is crucial for the appropriate choice of imaging strategy. Currently, most studies are using standard imaging procedures such as FLASH for feedback and localization.^[16,32] However, for this innovative use of MRI devices, the typical imaging sequences that are optimized for diagnostic imaging may not be the best choice. Therefore, there is also a need for developing new imaging sequences that are specially designed for the purposes of MRI-driven robotics.^[15] In parallel, exploring the advantages of additional assistive imaging techniques combined with MRI can provide higher

accuracy in navigation to the target site and treatment of the patient. For example, simultaneous PET/MRI systems are being used for diagnosis in preclinics for acquiring both anatomical (MRI) and functional (PET) information of tissues.^[88,89] The additional imaging modality introduced by the PET scanner provides more feedback information, which improves the capabilities of the MRI-driven robotics platform. Similarly, simultaneous imaging and actuation with MRI and ultrasound systems would open new capabilities for MRI-driven robotics.^[89,90] Furthermore, nanoprobes may offer an exciting opportunity for imaging microrobots inside MRI. Such multimodal imaging probes could be utilized to obtain high-resolution images of tissue in a highly localized region for precise operations.^[89,91]

7.2. Design Approach

In addition to the typical design requirements of medical robotics, such as size scale and biocompatibility, MRI-driven robot designs should also take specific magnetic field and gradient conditions of an MRI environment into consideration correctly. It is important to note that the strong and constant main magnetic field of MRI limits the motion degrees of freedom of robots, RF magnetic fields of the MRI device might result in undesired heating effects on the magnetic robots, and magnetic materials used on the robots would result in undesired MR image distortions locally. Potential MR safety issues should be considered as well. These robots should be steerable in MRI environments, provide localization and tracking signals for MRI-based feedback, and be well equipped (high enough force, reliable triggering mechanisms, etc.) to perform target medical functions. In this

perspective, exploring and expanding the robotic capabilities, while focusing on the requirements of a target medical task with already explored robotic tools and capabilities, would be a valuable asset for MRI-driven robot designs. Such design approaches would increase the capabilities and effectiveness of MRI-driven robots and make them more useful toward their clinical use.

7.3. Autonomy

MRI-driven robotic systems self-contain the components required to implement autonomous systems. These components are 1) state feedback and localization of the robot, 2) feedback of the target site to monitor the operation, 3) computation power for low- or high-level decision-making, 4) accepting and processing operator's inputs, and 5) actuating and controlling the robot for a set of autonomous tasks decided by the operator or the system itself. There are five autonomy levels in robotics, spanning from autonomy in low-level directives to fully autonomous and self-decision-making systems.^[87] Designing an autonomous robotic system requires choosing the proper autonomy level that best suits the medical needs and capabilities of MRI-driven robotics.

Based on the given medical tasks, the needs for autonomy may differ. For example, autonomous drug delivery in a vascular network has different autonomous needs than those of biopsy devices for stomach tumor diagnosis. Therefore, in addition to the level of autonomy, determining and developing robotic systems for the true autonomous needs of given medical tasks is crucial. Depending on the MRI systems, robot capabilities, and requirements of the desired task, the highest achievable level of autonomy might vary. Addressing and assessing the targeted level of

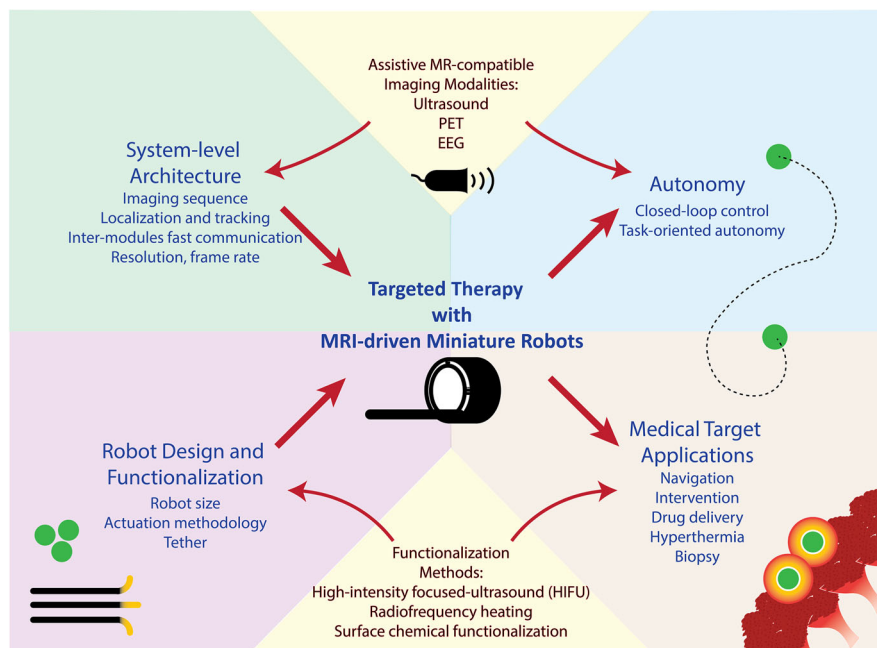


Figure 7. Utilizing MRI systems as a robotic platform could provide opportunities for new minimally invasive medical procedures and could increase the accuracy of the current medical operations. Combined with assistive MR-compatible imaging modalities, fine localization and continuous tracking of miniature robots, which are powered by the same MRI system, pave the way for safe and controlled minimally invasive medical operations in the human body. Properly designed and manufactured miniature robots show promise to accomplish potential given medical tasks (i.e., localized hyperthermia) with physical and computational intelligence under such robotic MRI systems.

autonomy for such technological advancements should be considered within the limits of the robotic system and the requirements of the medical task.

7.4. Improving Medical Functionalities

New medical functionalities could improve the usage of MRI-driven robots to reach the true potential of this field. Apart from navigation-related functionalities, medical functionalities can be encoded passively in the material properties of these robots. Functionalized surfaces of microrobots are used for realizing various medical functionalities, including tumor treatment and drug delivery.^[92,93] In such situations, MRI systems could be used as steering, navigation, and path-planning units, while the medical functionalization is realized through the smartly designed robot material. Combining MRI systems with radiofrequency heating or focused ultrasound units could render these systems to be used for imaging, actuation, and also triggering and controlling the temperature-based medical application via their already available (or external) RF fields, or with external focused ultrasound (FUS) waves toward cauterization and hyperthermia applications.

Finally, future studies should have a focus toward in vitro and in vivo studies. There have been a few studies using MRI-driven robots in in vitro and animal studies.^[11,33] These studies and tests are milestones before introducing this technology in medical centers, but they are not sufficient to prove the capability of using such robots in clinics yet. FDA and EMA guidelines and regulations should be followed carefully to translate MRI-driven robotics toward clinics. In addition, the aforementioned safety issues imposed by the magnetic field of MRI systems should be considered carefully for the clinical use of such robots.

In summary, clinical MRI systems can be used to image and actuate magnetic robots in difficult-to-reach regions of the human body. MRI-driven robotic systems can improve the controllability of the robots, which promotes surgeons to monitor and operate surgeries that require high precision and hand skill with high-level commands. Although the success rate and quality of surgeries could highly benefit from such technology in the future, there are unanswered questions in this newly emerging field of robotics. Improving robotic designs and medical capabilities with more precise imaging and localization as well as more robust system-level actuation and control would convert clinical MRI scanners into highly effective surgical operation rooms for high-precision minimally invasive operations in the future. In addition, the performance of such robots in medically relevant environments should be investigated further with animal experiments to pinpoint the true potential of MRI-driven robotics. The concepts discussed on the future outlook of MRI-driven robotic systems are summarized in **Figure 7**.

Acknowledgements

The authors thank Kaylen Richardson for her suggestions to improve the readability of the manuscript text. This work is funded by the Max Planck Society.

Conflict of Interest

The authors declare no conflict of interest.

Keywords

active catheters, magnetic actuation, magnetic resonance imaging, medical robotics, untethered miniature robots

Received: September 18, 2019

Revised: November 8, 2019

Published online: January 20, 2020

- [1] G. Z. Yang, J. Bellingham, P. E. Dupont, P. Fischer, L. Floridi, R. Full, N. Jacobstein, V. Kumar, M. McNutt, R. Merrifield, *Sci. Rob.* **2018**, 3, eaar7650.
- [2] M. W. Wilson, A. B. Martin, P. Lillaney, A. D. Losey, E. J. Yee, A. Bernhardt, V. Malba, L. Evans, R. Sincic, M. Saeed, *J. Vasc. Interv. Radiol.* **2013**, 24, 885.
- [3] OECD, *Health at a Glance*, OECD Publishing, Paris **2017**, p. 2017.
- [4] J.-B. Mathieu, G. Beaudoin, S. Martel, *IEEE Trans. Biomed. Eng.* **2006**, 53, 292.
- [5] A. Becker, O. Felfoul, P. E. Dupont, in *IEEE/RSJ Int. Conf. Intelligent Robots and Systems*, IEEE, Chicago, IL **2014**, p. 2017.
- [6] A. T. Becker, O. Felfoul, P. E. Dupont, in *IEEE Int. Conf. Robotics and Automation*, IEEE, Seattle, WA **2015**, p. 1184.
- [7] O. Felfoul, A. Becker, C. Bergeles, P. E. Dupont, *IEEE Trans. Rob.* **2015**, 31, 387.
- [8] P. Vartholomeos, C. Bergeles, L. Qin, P. E. Dupont, *Int. J. Rob. Res.* **2013**, 32, 1536.
- [9] P. Vartholomeos, L. Qin, P. E. Dupont, in *IEEE/RSJ Int. Conf. Intelligent Robots and Systems*, IEEE, San Francisco, CA **2011**, p. 4508.
- [10] G. Kósa, P. Jakab, G. Székely, N. Hata, *Biomed. Microdevices* **2012**, 14, 165.
- [11] J. Leclerc, A. Ramakrishnan, N. V. Tsekos, A. T. Becker, *IEEE Rob. Autom. Lett.* **2018**, 3, 403.
- [12] L. Arcese, M. Fruchard, A. Ferreira, in *IEEE/RSJ Int. Conf. Intelligent Robots and Systems*, IEEE, St. Louis, MO **2009**, p. 534.
- [13] A. Bigot, C. Tremblay, G. Soulez, S. Martel, *IEEE Trans. Rob.* **2014**, 30, 719.
- [14] O. Erin, J. Giltinan, L. Tsai, M. Sitti, in *IEEE Int. Conf. Robotics and Automation*, IEEE, Singapore **2017**, p. 3404.
- [15] O. Felfoul, A. T. Becker, G. Fagogenis, P. E. Dupont, *Sci. Rep.* **2016**, 6, 33567.
- [16] D. Folio, C. Dahmen, T. Wortmann, M. A. Zeeshan, K. Shou, S. Pane, B. J. Nelson, A. Ferreira, S. Fatikow, in *IEEE/RSJ Int. Conf. Intelligent Robots and Systems*, IEEE, San Francisco, CA **2011**, p. 1297.
- [17] F. P. Gosselin, V. Lalande, S. Martel, *Med. Phys.* **2011**, 38, 4994.
- [18] V. Lalande, F. P. Gosselin, S. Martel, in *IEEE/ASME Int. Conf. Advanced Intelligent Mechatronics*, IEEE, Montreal **2010**, p. 103.
- [19] V. Lalande, F. P. Gosselin, S. Martel, in *Int. Conf. IEEE Engineering in Medicine and Biology Society*, IEEE, Buenos Aires **2010**, p. 1874.
- [20] M. Latulippe, O. Felfoul, P. E. Dupont, S. Martel, *Appl. Phys. Lett.* **2016**, 108, 062403.
- [21] J. B. Mathieu, S. Martel, *Magn. Reson. Med.* **2010**, 63, 1336.
- [22] P. Pouponneau, J.-C. Leroux, S. Martel, *Biomaterials* **2009**, 30, 6327.
- [23] P. Pouponneau, J.-C. Leroux, G. Soulez, L. Gaboury, S. Martel, *Biomaterials* **2011**, 32, 3481.
- [24] T. Roberts, W. Hassenzahl, S. Hetts, R. Arenson, *Magn. Reson. Med.* **2002**, 48, 1091.

- [25] F. Settecase, M. S. Sussman, M. W. Wilson, S. Hetts, R. L. Arenson, V. Malba, A. F. Bernhardt, W. Kucharczyk, T. P. Roberts, *Med. Phys.* **2007**, *34*, 3135.
- [26] P. Vartholomeos, M. R. Akhavan-Sharif, P. E. Dupont, in *IEEE Int. Conf. Robotics and Automation*, IEEE, Saint Paul, MN **2012**, p. 1927.
- [27] E. Diller, J. Giltinan, G. Z. Lum, Z. Ye, M. Sitti, *Int. J. Rob. Res.* **2016**, *35*, 114.
- [28] E. Diller, J. Zhuang, G. Z. Lum, M. R. Edwards, M. Sitti, *Appl. Phys. Lett.* **2014**, *104*, 174101.
- [29] W. Hu, G. Z. Lum, M. Mastrangeli, M. Sitti, *Nature* **2018**, *554*, 81.
- [30] G. Z. Lum, Z. Ye, X. Dong, H. Marvi, O. Erin, W. Hu, M. Sitti, *Proc. Natl. Acad. Sci.* **2016**, *113*, E6007.
- [31] Z. Ye, M. Sitti, *Lab Chip* **2014**, *14*, 2177.
- [32] C. Dahmen, K. Belharet, D. Folio, A. Ferreira, S. Fatikow, *Int. J. Optomechatronics* **2016**, *10*, 73.
- [33] S. Martel, J.-B. Mathieu, O. Felfoul, A. Chanu, E. Aboussouan, S. Tamaz, P. Pouponneau, L. H. Yahia, G. Beaudoin, G. Soulez, *Appl. Phys. Lett.* **2007**, *90*, 114105.
- [34] M. Latulippe, S. Martel, in *IEEE RAS/EMBS Int. Conf. Biomedical Robotics and Biomechanics*, IEEE, São Paulo **2014**, p. 320.
- [35] M. Latulippe, S. Martel, *IEEE Trans. Rob.* **2015**, *31*, 1353.
- [36] A. Friedman, A. Liberzon, G. Kósa, in *IEEE Int. Conf. Robotics and Automation*, IEEE, Seattle, WA **2015**, p. 4736.
- [37] S. Kozerke, S. Hegde, T. Schaeffter, R. Lamerichs, R. Razavi, D. L. Hill, *Magn. Reson. Med.* **2004**, *52*, 693.
- [38] P. Magnusson, E. Johansson, S. Månsson, J. S. Petersson, C. M. Chai, G. Hansson, O. Axelsson, K. Golman, *Magn. Reson. Med.* **2007**, *57*, 1140.
- [39] N. Whiting, J. Hu, J. V. Shah, M. C. Cassidy, E. Cressman, N. Zacharias Millward, D. G. Menter, C. M. Marcus, P. K. Bhattacharya, *Sci. Rep.* **2015**, *5*, 12842.
- [40] O. Ocali, E. Atalar, *Magn. Reson. Med.* **1997**, *37*, 112.
- [41] M. Burl, G. A. Coutts, D. J. Herlihy, R. Hill-Cottingham, J. F. Eastham, J. V. Hajnal, I. R. Young, *Magn. Reson. Med.* **1999**, *41*, 636.
- [42] M. E. Ladd, G. G. Zimmermann, H. H. Quick, J. F. Debatin, P. Boesiger, G. K. von Schulthess, G. C. McKinnon, *J. Magn. Reson. Imaging* **1998**, *8*, 220.
- [43] M. E. Ladd, P. Erhart, J. F. Debatin, E. Hofmann, P. Boesiger, G. K. Von Schulthess, G. C. McKinnon, *Magn. Reson. Med.* **1997**, *37*, 891.
- [44] G. C. Mckinnon, J. F. Debatin, D. A. Leung, S. Wildermuth, D. J. Holtz, G. K. von Schulthess, *Magn. Reson. Mater. Phys. Biol. Med.* **1996**, *4*, 13.
- [45] M. Kaiser, M. Detert, M. A. Rube, A. El-Tahir, O. J. Elle, A. Melzer, B. Schmidt, G. H. Rose, *Biomed. Eng./Biomed. Tech.* **2015**, *60*, 89.
- [46] C. D. Jordan, B. R. Throne, A. Wadhwa, A. D. Losey, E. Ozhinsky, S. Kondapavulur, V. Fratello, T. Moore, C. Stillson, C. Yee, *IEEE Trans. Biomed. Eng.* **2019** <https://doi.org/10.1109/TBME.2019.2922879>.
- [47] A. Hai, V. C. Spanoudaki, B. B. Bartelle, A. Jasanoff, *Nat. Biomed. Eng.* **2019**, *3*, 69.
- [48] M. A. Rube, A. B. Holbrook, B. F. Cox, J. G. Houston, A. Melzer, *Magn. Reson. Imaging* **2014**, *32*, 693.
- [49] D. Ellersiek, H. Fassbender, P. Bruners, J. G. Pfeffer, T. Penzkofer, A. H. Mahnken, T. Schmitz-Rode, W. Mokwa, U. Schnakenberg, *Sens. Actuators, B* **2010**, *144*, 432.
- [50] H. Celik, A. Ulutürk, T. Tali, E. Atalar, *Magn. Reson. Med.* **2007**, *58*, 1224.
- [51] H. H. Quick, M. O. Zenge, H. Kuehl, G. Kaiser, S. Aker, S. Massing, S. Bosk, M. E. Ladd, *Magn. Reson. Med.* **2005**, *53*, 446.
- [52] T. Kuehne, R. Fahrig, K. Butts, *J. Magn. Reson. Imaging* **2003**, *17*, 620.
- [53] M. Burl, G. A. Coutts, I. R. Young, *Magn. Reson. Med.* **1996**, *36*, 491.
- [54] M. E. Miquel, S. Hegde, V. Muthurangu, B. J. Corcoran, S. F. Keevil, D. L. Hill, R. S. Razavi, *Magn. Reson. Med.* **2004**, *51*, 988.
- [55] A. Glowinski, G. Adam, A. Bucker, J. Neuerburg, J. J. van Vaals, R. W. Günther, *Magn. Reson. Med.* **1997**, *38*, 253.
- [56] A. Glowinski, J. Kursch, G. Adam, A. Bucker, T. G. Noll, R. Gunther, *IEEE Trans. Med. Imaging* **1998**, *17*, 786.
- [57] N. Olamaei, F. Cheriet, G. Beaudoin, S. Martel, in *Int. Conf. IEEE Engineering in Medicine and Biology Society*, IEEE, Buenos Aires **2010**, p. 4355.
- [58] O. Felfoul, J.-B. Mathieu, G. Beaudoin, S. Martel, *IEEE Trans. Med. Imaging* **2007**, *27*, 28.
- [59] M. P. Kummer, J. J. Abbott, B. E. Kratochvil, R. Borer, A. Sengul, B. J. Nelson, *IEEE Trans. Rob.* **2010**, *26*, 1006.
- [60] D. Son, M. D. Dogan, M. Sitti, in *IEEE Int. Conf. Robotics and Automation*, IEEE, Singapore **2017**, p. 1132.
- [61] R. Mhanna, F. Qiu, L. Zhang, Y. Ding, K. Sugihara, M. Zenobi-Wong, B. J. Nelson, *Small* **2014**, *10*, 1953.
- [62] D. R. Frutiger, K. Vollmers, B. E. Kratochvil, B. J. Nelson, *Int. J. Rob. Res.* **2010**, *29*, 613.
- [63] J. J. Abbott, O. Ergeneman, M. P. Kummer, A. M. Hirt, B. J. Nelson, *IEEE Trans. Rob.* **2007**, *23*, 1247.
- [64] D. Son, H. Gilbert, M. Sitti, *Soft Rob.* **2019** <https://doi.org/10.1089/soro.2018.0171>.
- [65] S. Yim, M. Sitti, *IEEE Trans. Rob.* **2012**, *28*, 1198.
- [66] C. Pawashe, S. Floyd, M. Sitti, *Int. J. Rob. Res.* **2009**, *28*, 1077.
- [67] Y. Kim, H. Yuk, R. Zhao, S. A. Chester, X. Zhao, *Nature* **2018**, *558*, 274.
- [68] Y. Kim, G. A. Parada, S. Liu, X. Zhao, *Sci. Rob.* **2019**, *4*, eaax7329.
- [69] O. Erin, H. B. Gilbert, A. F. Tabak, M. Sitti, *IEEE Trans. Rob.* **2019**, *35*, 1323.
- [70] T. Liu, N. L. Poirot, D. Franson, N. Seiberlich, M. A. Griswold, M. C. Çavuşoğlu, *IEEE Trans. Biomed. Eng.* **2016**, *63*, 2142.
- [71] F. Michaud, N. Li, R. Planteève, Z. Nosrati, C. Tremblay, K. Saatchi, G. Moran, A. Bigot, U. O. Häfeli, S. Kadoury, *Med. Phys.* **2019**, *46*, 789.
- [72] P. Moftakhar, P. Lillaney, A. D. Losey, D. L. Cooke, A. J. Martin, B. R. Thorne, R. L. Arenson, M. Saeed, M. W. Wilson, S. W. Hetts, *Radiology* **2015**, *277*, 842.
- [73] S. Hetts, M. Saeed, A. Martin, L. Evans, A. Bernhardt, V. Malba, F. Settecase, L. Do, E. Yee, A. Losey, *Am. J. Neuroradiol.* **2013**, *34*, 2083.
- [74] T. Liu, R. Jackson, D. Franson, N. L. Poirot, R. K. Criss, N. Seiberlich, M. A. Griswold, M. C. Çavuşoğlu, *IEEE/ASME Trans. Mechatron.* **2017**, *22*, 1765.
- [75] T. Greigarn, R. Jackson, T. Liu, M. C. Çavuşoğlu, in *IEEE Int. Conf. Robotics and Automation*, IEEE, Singapore **2017**, p. 3600.
- [76] T. Liu, N. L. Poirot, T. Greigarn, M. C. Çavuşoğlu, *J. Med. Devices* **2017**, *11*, 021004.
- [77] K. Zhang, A. J. Krafft, R. Umatham, F. Maier, W. Semmler, M. Bock, *Magn. Reson. Mater. Phys. Biol. Med.* **2010**, *23*, 153.
- [78] S. Hidalgo-Tobon, *Concepts Magn. Reson., Part A* **2010**, *36*, 223.
- [79] A. Chanu, O. Felfoul, G. Beaudoin, S. Martel, *Magn. Reson. Med.* **2008**, *59*, 1287.
- [80] A. Chanu, E. Aboussouan, S. Tamaz, S. Martel, in *Int. Conf. IEEE Engineering in Medicine and Biology Society*, IEEE, New York **2006**, p. 1746.
- [81] ICNIRP, *Health Phys.* **2017**, *112*, 305.
- [82] L. P. Panych, B. Madore, *J. Magn. Reson. Imaging* **2018**, *47*, 28.
- [83] ICNIRP, *Health Phys.* **2009**, *97*, 259.
- [84] ICNIRP, *Health Phys.* **2004**, *87*, 197.
- [85] FDA, *Guidance for Industry and Food and Drug Administration Staff*, U.S. Department of Health and Human Services, Rockville, MD, **2016**.

- [86] ISO, *Clinical Investigation of Medical Devices for Human Subjects: Good Clinical Practice*, International Organization for Standardization (ISO), Geneva **2011**.
- [87] G.-Z. Yang, J. Cambias, K. Cleary, E. Daimler, J. Drake, P. E. Dupont, N. Hata, P. Kazanzides, S. Martel, R. V. Patel, *Sci. Rob.* **2017**, *2*, 8638.
- [88] M. S. Judenhofer, H. F. Wehrl, D. F. Newport, C. Catana, S. B. Siegel, M. Becker, A. Thielscher, M. Kneilling, M. P. Lichy, M. Eichner, *Nat. Med.* **2008**, *14*, 459.
- [89] T.-H. Shin, Y. Choi, S. Kim, J. Cheon, *Chem. Soc. Rev.* **2015**, *44*, 4501.
- [90] F. A. Jolesz, *Annu. Rev. Med.* **2009**, *60*, 417.
- [91] P. Cai, W. R. Leow, X. Wang, Y. L. Wu, X. Chen, *Adv. Mater.* **2017**, *29*, 1605529.
- [92] M. Sitti, H. Ceylan, W. Hu, J. Giltinan, M. Turan, S. Yim, E. D. Diller, *Proc. IEEE* **2015**, *103*, 205.
- [93] H. Ceylan, J. Giltinan, K. Kozielski, M. Sitti, *Lab Chip* **2017**, *17*, 1705.
- [94] J.-B. Mathieu, S. Martel, L. H. Yahia, G. Soulez, G. Beaudoin, in *Int. Conf. IEEE Engineering in Medicine and Biology Society, IEEE, Cancun* **2003**, p. 3419.
- [95] P. Lillaney, C. Caton, A. J. Martin, A. D. Losey, L. Evans, M. Saeed, D. L. Cooke, M. W. Wilson, S. W. Hetts, *Med. Phys.* **2014**, *41*, 022305.